Engineering Fracture Mechanics 232 (2020) 107024

Contents lists available at ScienceDirect

Engineering Fracture Mechanics

journal homepage: www.elsevier.com/locate/engfracmech

Wedge splitting test of wood for fracture parameters estimation of Norway Spruce

Katarzyna Ostapska*, Kjell Arne Malo

NTNU, Department of Structural Engineering, Trondheim, Norway

ARTICLE INFO

Keywords:
Wood
Digital Image Correlation (DIC)
Wedge split test
Crack growth
Fracture energy
Stress intensity factor
R-curves
Pattern search method

ABSTRACT

Crack evolution in wood from Norway Spruce during mode I wedge splitting tests was measured using a Digital Image Correlation (DIC) system. The resulting series of deformation fields were post-processed in order to obtain kinematically based crack tip location histories throughout the loading procedure, by a purposely made algorithm. The developed algorithm is based on generic mode patterns which are fitted to the observed deformation fields and optimized. The developed procedure and its application are explained and the resulting crack paths are presented. Subsequently, fracture energies, critical stress intensity factors and experimental resistance curves were derived based on the crack path data. Comparisons of the obtained material parameters for fracture mechanics with literature values show that the proposed method is a powerful alternative to the more traditional methods. Moreover, experimentally derived crack tip location histories give more detailed insight into the behaviour of wood (Norway Spruce) during mode I fracture and may replace indirect methods and crack length assumptions.

1. Introduction

1.1. Motivation for fracture testing of wood

Wood is a challenging material to describe with the means of material mechanics, primarily due to its natural origin that precludes production control. Moreover, the organic origin of wood hampers the effort toward achieving a satisfactory level of behaviour repeatability and, in consequence, its predictability. As nature engineered composite, wood is especially challenging when it comes to fracture mechanics. Each of the three basic modes of failure can occur in six different configurations of material orientation, eighteen basic modes of failure; some of them are depicted in Fig. 1. However, due to the highly orthotropic nature of wood, certain modes can be distinguished as a leading cause of material failures. Among those are splitting along the grain: Mode I RL and Mode I TL. Those types of failure are the governing mechanisms in structural collapse occurring especially in notched beams and beams with holes, where the concentration of perpendicular to grain stresses is augmented by the chosen design and may lead to delamination. Furthermore, in dowel type joints, the splitting is caused by wedge-like behaviour of dowels, that, although being loaded predominantly in the direction along the grain, can introduce relatively high stresses acting perpendicular to the grain. Careful investigation of the mechanism of fracture initiation, development and propagation gives more insight into the structural performance of timber structures, enhances reliability and facilitates the design process. The fracture behaviour of Norway Spruce and other wood species has been described with the means of methods developed for other materials; mainly steel, concrete, and engineered composites.

* Corresponding author.
E-mail address: katarzyna.ostapska-luczkowska@ntnu.no (K. Ostapska).

https://doi.org/10.1016/j.engfracmech.2020.107024
Received 17 August 2019; Received in revised form 18 March 2020; Accepted 22 March 2020
Available online 22 April 2020

Nomenclature

(r, ϕ) and (x, y)	polar coordinate system axes and Cartesian coordinate system axes
α_i	perturbation
κ	Kolosov's constant/parameter
f_i, g_i, l_i, m_i	polar functions
ν_{RL}, ν_{TL}	Poisson's ratio on planes Radial-Longitudinal and Tangential-Longitudinal
A	coefficients of the power series
P	set of perturbed values
S	matrix defining perturbation pattern for optimized parameter vector
u	experimental displacement field
v	vector of optimized parameters
θ	wedge angle between vertical direction and inclined side
A_c	fracture surface area
a_{ini}	initial crack length
e	error
E_L, E_R, E_T	Young's modulus in longitudinal, radial and tangential direction
F_h, F_v	horizontal and vertical force
G_c	Cumulative released energy
$G_{F,crit}$	critical fracture energy
$G_{F,cum}$, $G_{F,cum,tot}$	specific fracture energy, total specific fracture energy (cumulative)
$G_{F,res}$	fracture resistance at the final crack slope
G_j	Fracture energy
$K_{I,c}$, K_I	Critical stress intensity factor and stress intensity factor in mode I
R	Resistance to fracture: R-curve
T_x, T_y, R	rigid body motions
v, δ	vertical displacement, horizontal displacement: crack opening displacement - COD
x_0, y_0	crack tip location coordinates - start point

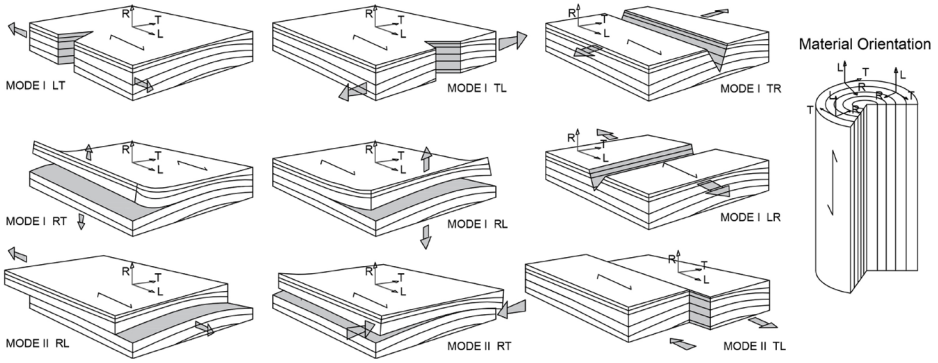

Fig. 1. Selected modes of failure in wood. Material orientation of fracture surface is defined by two letters, e.g. in RL, fracture plane is orthogonal to R material direction and crack propagates in the L material direction. Material directions are depicted on the right for wood log: R- radial, T-tangential, L- longitudinal.

However, the heterogeneous nature of wood requires careful interpretation and adjustments. For structural purposes, the fracture process at the proper scale needs to be considered. Furthermore, special attention has to be put to the crack propagation process. The fracture in wood, as in other materials, is driven by the underlying micro-mechanism of failure [1,22,5]. In the splitting along the grain, this is mainly the lignin matrix fracture between fibres combined with through-cell tearing. Different heterogeneities, e.g. knots, deviations in the direction of grain and growth ring irregularities, result in the non-smooth force-displacement experimental curves. It is natural to expect that the crack tip propagation also reflects the same heterogeneities, corresponding to the fluctuations in the force-displacement curves.

1.2. Description of existing test methods

A method for crack tip localization needs to be employed in order to estimate crack length during the wedge split test procedure. Most widely used methods are compliance-based crack length estimation [4], visual assessment of subsequent crack images [30], strain observation based on DIC [14] and image processing of crack images [20]. The compliance-based method for crack length estimation is indirectly based on experimental data and requires, in addition, assumptions of the material behaviour. Strain tracking based on an a priori selected limit value is a very straightforward method but is also limited to the small observation zone and therefore may be affected by local effects. Methods based on image analysis are directly dependent on experimental data, and crack tip localization requires comparative studies of very small areas on numerous subsequent images. For heterogeneous materials exhibiting fracture process zones, this method can be quite complicated. Moreover, the observation of the crack tip on the surface is restricted to the small zone and for the specimen with substantial depth to width ratio, this may not reflect the global behaviour of the specimen, but capture only local effects instead.

2. Materials and methods

2.1. Experimental test setup

The wedge splitting test was introduced in [12] by Tschegg and Linsbauer as a new method for measurement of fracture energy of concrete materials in mode I. The splitting force is obtained by using a wedge with a small angle, transferring the relatively small vertical force into a larger horizontal force component. The load is transferred by roller bearings to ensure negligibly low frictional forces. In the present work, the steel wedge has $2\theta = 20°$ angle and transfers the load from the load cell to the specimen through steel rollers connected to the L-shape profiles resting on the specimen, see Fig. 2. The horizontal force component can be calculated from a simple force equilibrium, Eq. (1).

$$F_h = \frac{F_v}{2 \cdot \tan\theta} \tag{1}$$

The crack opening displacement (COD) is calculated from the vertical extension measurement v with a simple formula $\delta = 2v \cdot \tan\theta$. The COD δ is used to calculate the work of the horizontal force component F_h, which equals the cumulative released energy G_c during wedge split test, Eq. (2), where δ_f is COD at failure and $0 < \delta_0 < \delta_f$.

$$G_c = \int_0^{\delta_0} F_h d\delta - \frac{F_h \delta_0}{2} \rightarrow G_{c,tot} = \int_0^{\delta_f} F_h d\delta \tag{2}$$

The energy, related to the vertical force component, is assumed small and negligible. However, its possible influence is evaluated with regard to the numerically obtained Stress Intensity Factor (SIF). The specific fracture energy is defined as cumulative released energy divided by corresponding fracture surface: $G_{F,cum} = \frac{G_c}{A_c}$.

2.2. Specimen

The specimens were cut from glue-laminated timber of class GL30c [7], with lamella thickness 45 mm. Two series of specimens were prepared to test fracture in RL (Radial-Longitudinal) and TL (Tangential-Longitudinal) plane, see Fig. 3. The first subscript refers to the direction normal to the fracture plane and the second refers to the direction of crack propagation. The general dimensions, as depicted in Fig. 2a are: H = 300 mm, B = 225/230 mm, W = 140/135 mm. The machined cuts were designed to allow the transfer of the splitting force without introducing bending moments on the specimen arms and stress concentrations in areas outside the notch. The notch is a 10 mm deep and 3 mm wide groove. The resulting ligament length L is 180 mm. As the thickness of the specimen encompasses the whole width of the glue-laminated beam, the knots, drying cracks and other defects are inherent material properties. The fracture zone is located in the inner boards of strength class T15 [19]. The crack propagates along the grain direction across the width of one board W = 140 mm for specimens in the RL series and across the thickness W = 135 mm of 3 boards for specimens in the TL series. The total nominal fracture surface equals $A_{c,RL} = LW = 252\ \text{cm}^2$, $A_{c,TL} = LW = 243\ \text{cm}^2$. The mode of failure is nominally mode I RL and TL, but in practice, it is a mix of Mode I RL and Mode I TL, especially in the RL series, as typically

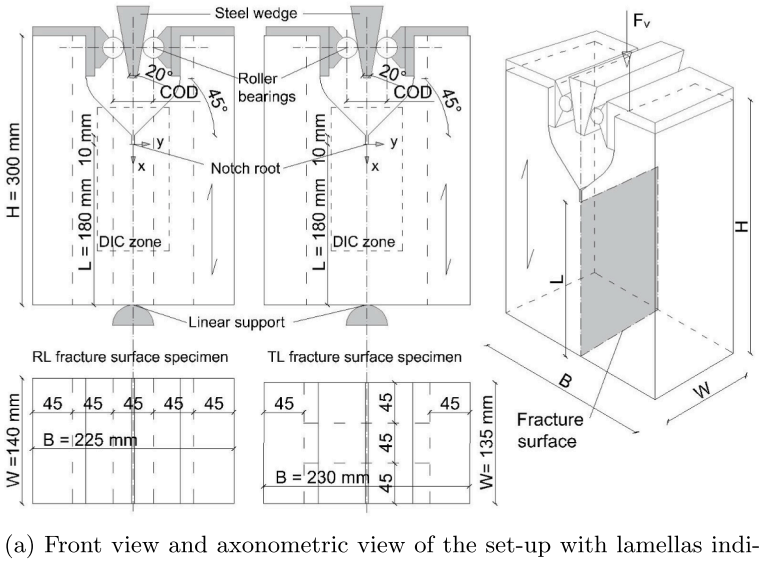

(a) Front view and axonometric view of the set-up with lamellas indicated by dashed lines.

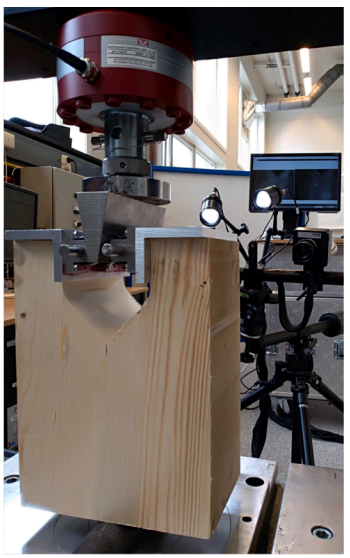

(b) Experimental setup with DIC cameras

Fig. 2. Wedge split test: specimen dimensions (a) and set-up view (b).

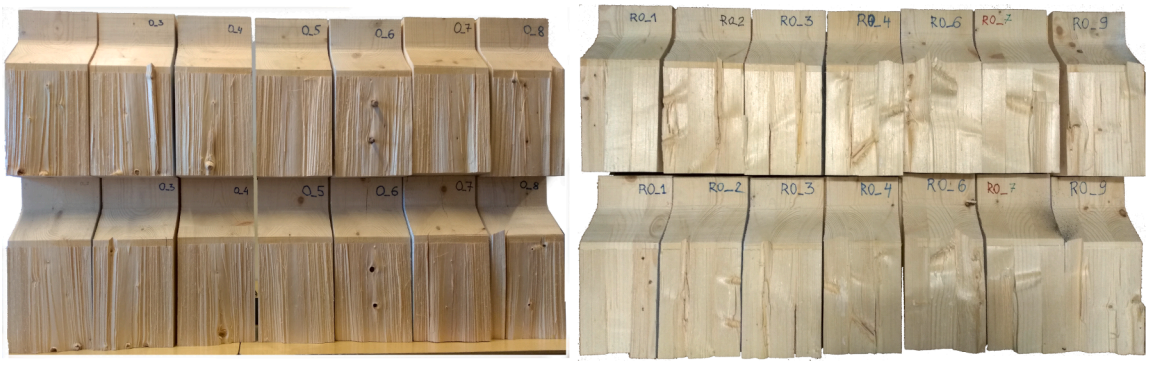

(a) RL specimens (b) TL specimens

Fig. 3. Fracture surfaces from wedge-split test specimens.

occurring in timber structures. Moreover, mode II is expected to be present as the grain angle variation and general material variability make pure mode I condition impossible in practice. The grain angle was measured on specimens in both series and its mean value is 1.5° with 58% COV for RL orientation and 1.9° with 61% for TL. The detailed data are attached in the Appendix A. Before testing, the specimens were stored in a climate room with relative humidity 65% and temperature 20° which resulted in the 12–13% moisture content (MC).

2.3. Loading procedure

The specimens are tested using a universal testing machine (INSTRON model No 5982) with a maximum capacity of 100 kN. The test is run in position control and both displacement and corresponding measured force are recorded and synchronized with all other measurements. The crosshead speed was 1 mm/min for the initial loading stage up to $\delta = 5$ mm displacement, and then the speed was reduced to $v = 0.1$ mm/min to ensure stable crack growth. The specimens were repeatedly unloaded and reloaded with a speed of 1 mm/min at different stages with reference to the maximum peak force. A typical loading procedure is shown in Fig. 4. The analog-to-digital converter (ADC) applied for signal digitalization has a resolution of 14 bits; resulting in 12.2 N load resolution and 6.1 μm displacement resolution (with max displacement set to 100 mm). The MC of the specimens were checked by control of the mass before and at the end of the tests and the resulting loss in mass was 0.13% on average, which corresponds to a drop in MC by 1.1%.

2.4. DIC characteristics

The deformations on the surface around the notch and in the zone of crack propagation (see DIC zone in Fig. 2a) were measured by means of digital image correlation (DIC) using ARAMIS system with 4 M (2048 × 2048 pixels) cameras. The surfaces of the specimens were covered with stochastic patterns to ensure the quality of the recorded images. The measured area, DIC zone in Fig. 2a, was approximately 80 mm wide and 160 mm high. The effective resolution of the measured area is approximately 0.1 mm/pixel and calibration accuracy is 0.04 pixels, giving the estimated displacement resolution of about 0.004 mm. However, considering the

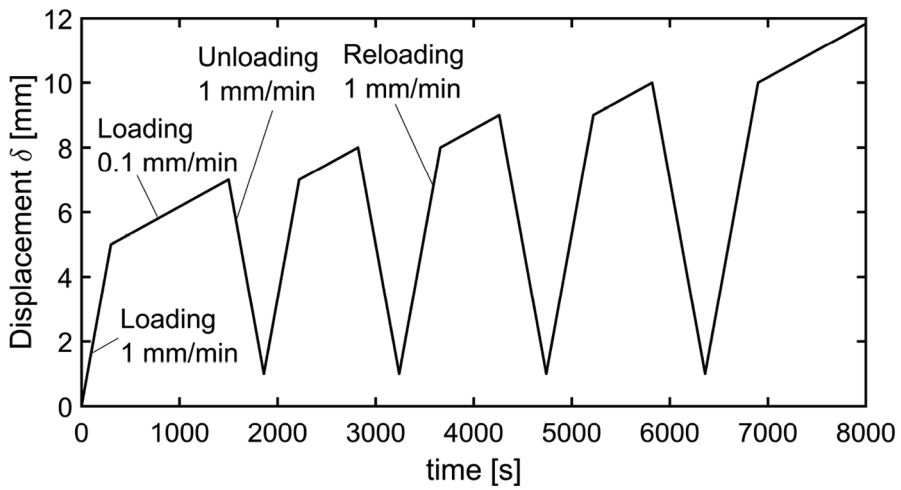

Fig. 4. Typical loading procedure for Wedge Split Test with unloading-reloading paths.

typical smallest measurable displacement in DIC systems of approximately 0.1 pixels, the measured displacement resolution is 0.01 mm. The images were recorded with a frequency of f = 0.2 Hz. This corresponds to vertical displacement increments of around $\Delta_v = v/60/f = 0.008$ mm and an increment in COD: $\Delta_{COD} = 0.00141$ mm between subsequent images. The DIC measurements were synchronized with the loading scheme by analog signal inputs both for displacements and force for every recorded image.

2.5. Crack tip localization

Localization of the crack tip in wood is a non-trivial task and several factors need to be considered. First of all, wood is a fibrous material and fibres are bridging the cracking zone during the fracture process, thus contributing to the total fracture energy of the material. The fibre bridging zone (FBZ) is located between two crack tip locations, the notch root and the actual crack tip at the front of FBZ [18]. For the crack to initiate and propagate, micro-cracking between many fibres has to occur. Due to variations in fibre properties and orientations across the wood cross-section and general inhomogeneity of wood, micro-cracking occurs in a finite zone rather than at a point [25,24]. Since the width of the specimens is substantial in comparison to other dimensions, the localization of the crack tip position based on simple visual observations of the surface with regard to the crack appearance can be misleading. In addition, small deformations in the FBZ make the visual identification of the crack tip cumbersome. In the present paper, an approach to localize and follow the crack tip location is proposed. The method is based on analyses of the deformation fields obtained with DIC for a series of loading stages throughout the whole wedge splitting test. The method employs series expansion of the displacement field that is kinematically admissible for complex potential function solution of 2D plane stress/strain crack problems. The higher-order terms of a series exapnsion account for the higher strain fields at a distance from the crack tip asymptotic stress, see [17,13,31,10]. Firstly, a decomposition of the kinematic field into the mode I - opening, and mode II - shearing, is realised by the use of the analytical description proposed by Kolosov-Mushkelishvili, formulated by Eq. (3), and described in [31,6,15,11,16]. The experimental displacement field $\mathbf{u} = [u_x^1 .. u_x^k .. u_x^M \; u_y^1 .. u_y^k .. u_y^M]^T$ obtained with DIC is modelled by a series expansion formulated by Eq. (3) for each point k, where index $k = 1..M$ refers to a deformation field point measured with DIC, and subscripts x, y refer to displacement directions. In a coordinate system where the x-axis is aligned with crack propagation direction u_x and u_y represent shear and opening modes, respectively. The approximations are made by the use of power series of polar functions f_i, g_i, l_i, m_i (as defined in Eqs. (6a)–(6d).

$$\mathbf{u}^k = \begin{bmatrix} u_x^k \\ u_y^k \end{bmatrix} = \sum_{i=1}^{N} \left\{ \begin{bmatrix} f_i(\kappa, \phi_k) & g_i(\kappa, \phi_k) \\ l_i(\kappa, \phi_k) & m_i(\kappa, \phi_k) \end{bmatrix} \begin{bmatrix} A_1^i \\ A_2^i \end{bmatrix} r_k^{i/2} \right\} + \begin{bmatrix} T_x \\ T_y \end{bmatrix} + R \begin{bmatrix} y_k \\ x_k \end{bmatrix} \tag{3}$$

The $2{\cdot}N$ coefficients of the power series: $\mathbf{A}^T = [A_1^1 ... A_1^N A_2^1 ... A_2^N]$, Eq. (3), are scaling the even (subscript 1) and odd (subscript 2) polar functions and thus inform about mode I and II composition respectively. The polar coordinates of point k (r_k, ϕ_k) are defined in Eqs. (4) and (5) respectively. T_x, T_y, R are corrections for rigid body motions. Cartesian coordinates x_k, y_k of point k are obtained from the DIC measurement and the deformation field is related to the crack tip origin: x_0, y_0.

$$r_k = \sqrt{(x_k - x_0)^2 + (y_k - y_0)^2} \tag{4}$$

$$\phi_k = \begin{cases} \operatorname{acos}(\frac{x_k - x_0}{r_k}) & \text{if } y > 0 \\ -\operatorname{acos}(\frac{x_k - x_0}{r_k}) & \text{if } y < 0 \\ \textit{undefined} & \text{if } y = 0 \end{cases} \tag{5}$$

The polar functions for term i are computed from:

$$f_i(\kappa, \phi_k) = (\kappa + \frac{i}{2} + (-1)^i) \cdot \cos(\frac{i}{2} \cdot \phi_k) - \phi_k \cdot \frac{i}{2} \cdot \cos(\frac{i}{2} - 2) \tag{6a}$$

$$g_i(\kappa, \phi_k) = (-\kappa - \frac{i}{2} + (-1)^i) \cdot \sin(\frac{i}{2} \cdot \phi_k) + \phi_k \cdot \frac{i}{2} \cdot \sin(\frac{i}{2} - 2) \tag{6b}$$

$$l_i(\kappa, \phi_k) = (\kappa - \frac{i}{2} - (-1)^i) \cdot \sin(\frac{i}{2} \cdot \phi_k) + \phi_k \cdot \frac{i}{2} \cdot \sin(\frac{i}{2} - 2) \tag{6c}$$

$$m_i(\kappa, \phi_k) = (\kappa - \frac{i}{2} + (-1)^i) \cdot \cos(\frac{i}{2} \cdot \phi_k) + \phi_k \cdot \frac{i}{2} \cdot \cos(\frac{i}{2} - 2) \tag{6d}$$

The Kolosov's constant κ is a coefficient that corrects the kinematic field for the assumptions of plane strain $\kappa = 3 - 4\nu$, or plane stress $\kappa = (3 - \nu)/(1 + \nu)$, where ν denotes the relevant Poisson's ratio. In the case of cylindrical orthotropic material κ cannot be decided a priori and an optimization procedure has been employed to determine its value. Therefore, Kolosov's constant is treated here as a parameter and can only be connected to the material properties within the elastic range of load. Ideally, the LEFM for orthotropic materials and with higher-order terms should be employed. A certain initial value based on typical Poisson's ratio for wood: $\nu_{RL,TL} = 0.4 - 0.5$ can be used as the first estimate of the field. By choosing a reasonable start point x_0, y_0 and value of κ the first solution for $\mathbf{X}^T = [A_1^1 ... A_1^N A_2^1 ... A_2^N \; T_1 \; T_2 \; R]$ can be obtained by solving $\mathbf{u} = \mathbf{b}{\cdot}\mathbf{X}$, where $\mathbf{b}$ is a matrix built of the polar functions and the coordinates for each point $k = 1..M$, see Eq. (7), and $\mathbf{u}_k = \mathbf{b}_k{\cdot}\mathbf{X}_k$ is shown fully in Eq. (3).

$$\mathbf{b} = \begin{bmatrix} r_1^{0.5}\mathrm{f_1}(\kappa,\phi_1) & r_1^{0.5}\mathrm{g_1}(\kappa,\phi_1) & \dots & r_N^{0.5}\mathrm{f_N}(\kappa,\phi_M) & r_N^{0.5}\mathrm{g_N}(\kappa,\phi_1) & 1 & 0 & -y_1 \\ \vdots & \vdots & \vdots & \vdots & \vdots & \vdots & \vdots & \vdots \\ r_M^{N/2}\mathrm{f_1}(\kappa,\phi_M) & r_M^{N/2}\mathrm{g_1}(\kappa,\phi_M) & \dots & r_N^{N/2}\mathrm{g_N}(\kappa,\phi_M) & r_N^{N/2}\mathrm{g_N}(\kappa,\phi_M) & 1 & 0 & -y_M \\ r_1^{0.5}\mathrm{l_1}(\kappa,\phi_1) & r_1^{0.5}\mathrm{m_1}(\kappa,\phi_1) & \dots & r_N^{0.5}\mathrm{l_1}(\kappa,\phi_M) & r_N^{0.5}\mathrm{m_N}(\kappa,\phi_1) & 0 & 1 & x_1 \\ \vdots & \vdots & \vdots & \vdots & \vdots & \vdots & \vdots & \vdots \\ r_M^{N/2}\mathrm{l_1}(\kappa,\phi_M) & r_M^{N/2}\mathrm{m_1}(\kappa,\phi_M) & \dots & r_N^{N/2}\mathrm{l_1}(\kappa,\phi_M) & r_N^{N/2}\mathrm{m_N}(\kappa,\phi_M) & 0 & 1 & x_M \end{bmatrix} \tag{7}$$

The goodness of the first approximation of $\mathbf{u}^T_{Fitted} = [u_{x,Fitted}\ u_{y,Fitted}]$, is evaluated with the error function as defined by Eq. (8).

$$e = \frac{\sum_{k=1}^{M}\sqrt{(u^k_{x,Fitted} - u^k_{x,exp})^2 + (u^k_{y,Fitted} - u^k_{y,exp})^2}}{M} \tag{8}$$

The error at each point k is averaged over the number of points M. Furthermore, the error function is used as an error function in an optimization procedure for ultimate crack tip localization and for determination of κ. The pattern search method has been selected, as this method belongs to the group of direct search methods. It has a zero-order rate of convergence, and is widely known and universally applicable. The advantage of using a pattern search method is the high accuracy and simplicity of the algorithm. Pattern search methods do not require gradient computation and are less sensitive to the initial start point selection, as was shown in [32]. Moreover, the speed of the method can be increased by an improved initial guess. This is achieved in the algorithm described in the present paper, by utilisation of the last found crack tip location, as a starting point for the subsequent step. The procedure for localization of the crack path from the set of deformation fields of subsequent load stages is schematically depicted in Fig. 5. An example of optimized displacement fields of each deformation mode is depicted in Fig. 6 for two stages of loading: namely the maximum splitting force and post-peak splitting force.

The pattern search algorithm, in its original form described by Hooke and Jeeves [9], consists of two parts: the exploratory search and the pattern move. In the exploratory search a small perturbation α_i of the optimized parameters $\mathbf{v}$ is introduced with a pattern defined by matrix $\mathbf{S}$, see Eq. (9). For the considered field the vector of parameters for optimization is: $\mathbf{v} = [x_0\ y_0\ \kappa]$. A set of perturbed values $\mathbf{P}$ is constructed, Eq. (9), and for each set of perturbed values (each row in $\mathbf{P}$) the error function, Eq. (8), is evaluated. The perturbation of vector $\mathbf{v}$ that minimizes the error function (Eq.(8)) $P_{min} = \min(P)$ is used as the new starting point. The perturbation continues anew with an increased step size. If no set of perturbed values minimizes the error function, the perturbation size is decreased and the procedure is restarted at the same point $\mathbf{v}$. The algorithm runs until the error function is sufficiently minimized or until no change is achieved after a given number of perturbation cutbacks. For the present optimization procedure the initial perturbations were set to $\alpha_1 = \alpha_2 = \alpha = 0.05$ for x_0, y_0, and $\alpha_3 = \alpha/10$ for κ. Stopping criteria were $e <= 0.001$ and $\alpha < 10e - 6$.

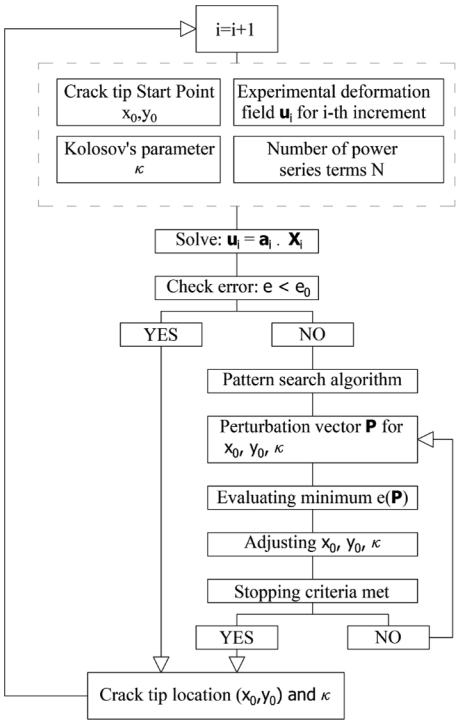

Fig. 5. Crack tip localization procedure.

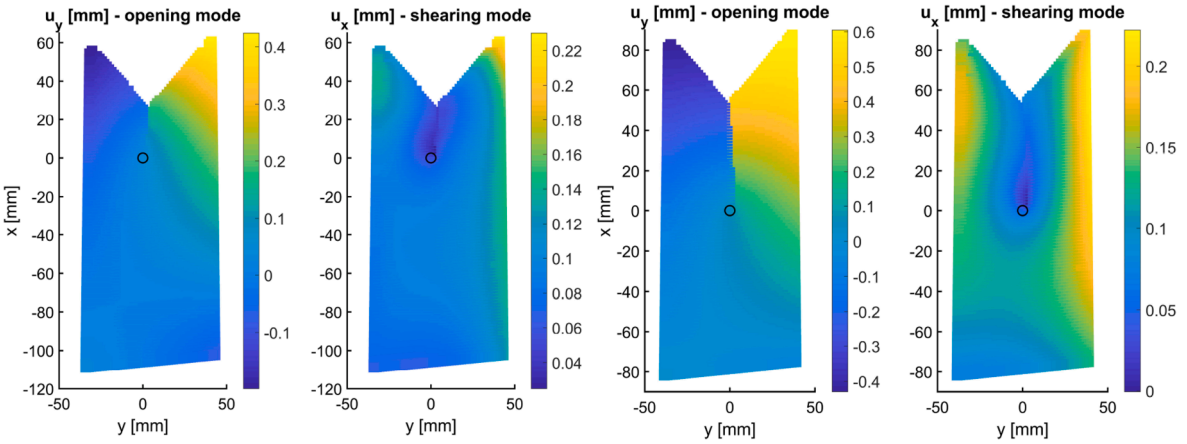

(a) Maximum splitting force:$F_h = 1711N$ (b) Post-peak splitting force: $F_h = 1207N$

Fig. 6. Adjusted deformation field maps for mode I and mode II in specimen no 6 (*WST* – 08) for pre (a) and post (b) crack initiation stages.

$$\mathbf{P} = \begin{bmatrix} x_0 & y_0 & \kappa \\ x_0 & y_0 & \kappa \\ x_0 & y_0 & \kappa \\ x_0 & y_0 & \kappa \\ x_0 & y_0 & \kappa \\ x_0 & y_0 & \kappa \end{bmatrix} + \begin{bmatrix} \alpha_1 & 0 & 0 \\ 0 & \alpha_2 & 0 \\ 0 & 0 & \alpha_3 \\ -\alpha_1 & 0 & 0 \\ 0 & -\alpha_2 & 0 \\ 0 & 0 & -\alpha_3 \end{bmatrix} = \begin{bmatrix} \mathbf{v} \\ \mathbf{v} \\ \mathbf{v} \\ \mathbf{v} \\ \mathbf{v} \\ \mathbf{v} \end{bmatrix} + \begin{bmatrix} \mathbf{S} \\ \mathbf{-S} \end{bmatrix} \tag{9}$$

Typical error functions evaluated along the crack path for a series of subsequent deformation fields are shown in Fig. 7.

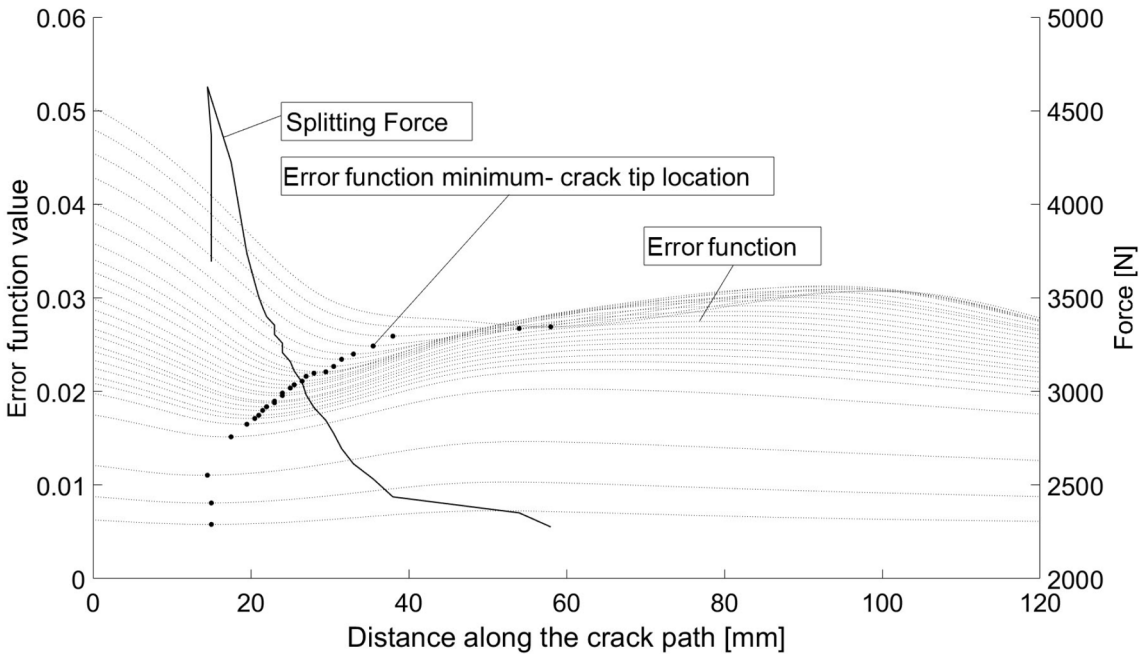

Fig. 7. Example of error function along the crack path distance for different stages of splitting test. The minima of error functions are depicted with black dots. The splitting force F_h is plotted on the right vertical axis.

2.6. Fracture energy evaluation

The fracture energy G_j was calculated by numerically integrating the area under the graph of the horizontal (splitting) force F_h versus the crack opening displacement (COD), as depicted in Fig. 8. The energy stored in elastic deformation was subtracted assuming that, in the absence of fibre bridging, the unloading path would return to the initial point, e.g. point A in Fig. 8, as explained in [30]. The cumulative fracture energy G_c represents values of G_j for all discrete $F_h - COD$ points. The cumulative fracture energy G_c was divided by the corresponding cracked area, giving the specific fracture energies $G_{F,cum}$, which were evaluated for two distinct points: at the COD corresponding to the last retrieved crack tip location from DIC (see $G_{F,cum}$ in Fig. 9 and Figs. B.13 and B.14 in Appendix B), and at the end of the test, where the crack was measured manually ($G_{F,cum,tot}$ in Figs. 9, B.13 and B.14). The determined values are listed in Table 1 for RL series and in Table 2 for TL series.

The resistance of wood against crack propagation was estimated for the range of COD where the crack tip was located by the use of the described algorithm for analysis of DIC measurements. The crack length a was measured as the distance between the optimized crack tip and notch root (the origin of the coordinate system, e.g. in Fig. 2a), thus it includes the initial crack a_{ini}. To evaluate the resistance, least-square spline approximations of the curve a and G_c were utilized. The polynomial order was set to one giving piecewise-linear approximations, (G_c: lin. app. and a: lin. app. in Figs. 9, B.13 and B.14).

The spline knots (endpoints of linear pieces) were specifically chosen for each specimen, so as to follow the jumps and drops in the curves. For each piece of the linear approximation of the G_c and the corresponding linear approximation of the a, the slope ratio was evaluated $R = \frac{\Delta G_c}{\Delta a}$. The resulting piecewise constant resistance curve was plotted against crack length a, see R-curve in Figs. 9, B.13 and B.14.

2.7. Stress intensity factor

The stress intensity factor (SIF) for the wedge split specimen was obtained by using plane stress/strain finite element analysis (FEA) with a contour integral method for orthotropic materials. The model was created in ABAQUS [23]. Both plane stress and plane strain elements were utilized, and several crack lengths were evaluated to obtain SIF (K_I for mode I) in the function of initial crack length ratio to the ligament length: $\frac{a_{ini}}{L}$. The initial crack length a_{ini} was obtained with the crack tip localization procedure based on the DIC measurements. The modelling approach was validated by using the well-known solution for CT (Compact Tension) specimen [28]. Discrete data from FEA of WST for both plane stress and plane strain elements are plotted in Fig. 10 together with CT solution. The SIF for the WST specimen is dependent on the specimen geometry and boundary conditions, which is accounted for by the dimensionless function $f(a_{ini}/L)$. The data points are interpolated linearly, which for $a_{ini}/L < 0.5$ is judged sufficiently accurate estimation of f. The classic linear elastic fracture mechanics (LEFM) formula for K_I is given by Eq. (10).

$$K_I = \frac{P}{W\sqrt{L}} f\left(\frac{a_{ini}}{L}\right) \tag{10}$$

Moreover, a typical mesh with spider web design, used in ABAQUS simulations, is depicted on the right of Fig. 10. The plane strain elements give on average 2% higher stress intensity factors compared to plane stress elements. The influence of the vertical component of the force was also investigated. The results from the numerical analysis show that the SIF value increases by 2% with an added vertical load of approximately 20% value of the horizontal splitting force. Based on the numerical results, the experimental critical stress intensity factors K_{Ic}, Eq. (10), were evaluated by using maximum splitting force P_{max} and the corresponding initial crack a_{ini} from experimental data optimization, see Tables 1 and 2. The equivalent fracture toughness measure $G_{F,crit}$ for mode I in classic LEFM can be obtained from the formula relating the fracture energy G_F with SIF K_I, valid for rectilinearly orthotropic bodies with a crack path along a material symmetry plane [21], Eq. (11).

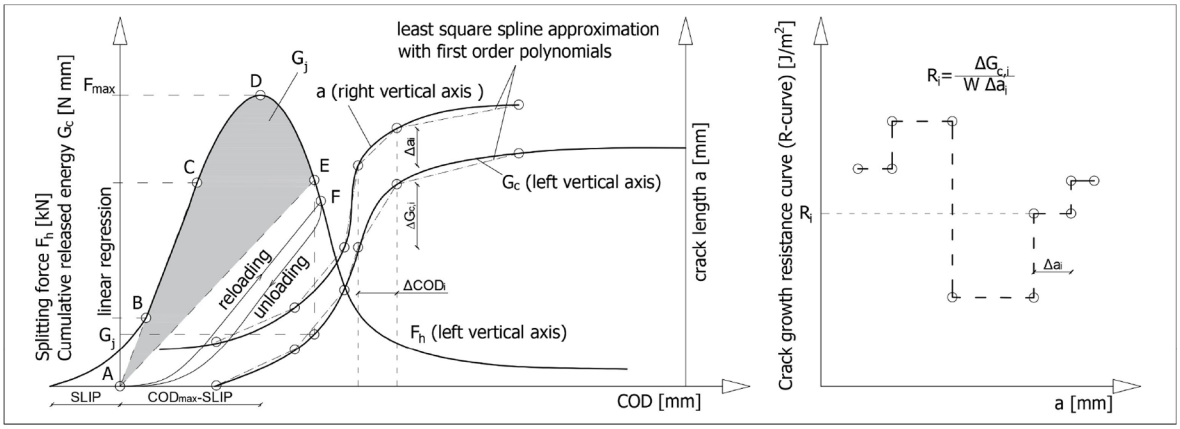

Fig. 8. Fracture energy evaluation procedure.

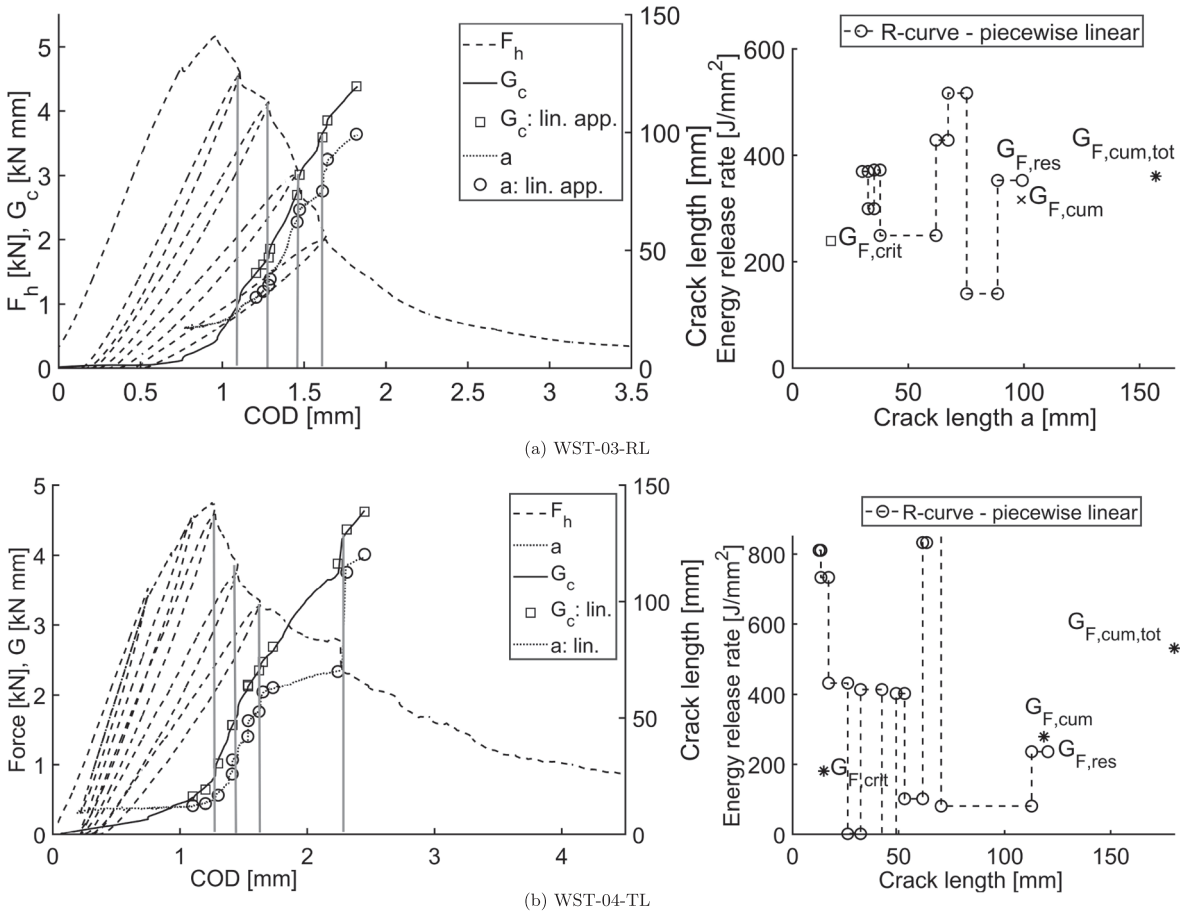

Fig. 9. Results for selected specimens from both series. Left: Force-displacement curve, cumulative fracture energy G_c, crack length a, lin. app. - piecewise linear approximation; Right: energy release rate (R-curve). Vertical lines on the left graphs indicate locations of unloading-reloading cycles and corresponding drops in force and energy and jumps in crack length. Naturally occurring jumps are captured as well, see last vertical line in left b.

Table 1
Fracture properties obtained from analysis of WST experiments in RL.

SPECIMEN ID: WST- SPECIMEN NO		02-RL 1	03-RL 2	04-RL 3	05-RL 4	06-RL 5	07-RL 6	08-RL 7	mean	COV [%]
$P_{h,max}$		4804	5167	4637	4218	4287	3736	4591	4491	11
$COD_{max} - SLIP$ [mm]		1.03	0.97	0.91	1.07	1.08	0.95	1.14	1.02	9
K_{Ic}	a_{ini} (DIC)	0.52	0.55	0.47	0.43	0.48	0.38	0.45	0.47	12
[MPa m$^{0.5}$]	a_{ini} = 10 mm	0.45	0.49	0.44	0.40	0.41	0.36	0.44	0.43	11
a_{ini} from DIC [mm]		20.3	20.0	16.6	15.8	25.6	15.7	13.7	18.25	24
Rigid body	T_x [mm]	0.0027	0.0017	0.0130	0.0124	0.0044	0.0071	0.0362	0.011	113
	T_y [mm]	0.0923	0.0311	0.0462	0.0124	0.2843	0.0469	0.0437	0.080	128
	R [rad]	0.0019	0.0014	0.0012	0.0017	0.0022	0.0018	0.0027	0.002	29
Def. Mode	A_1^1	0.0256	0.0211	0.0190	0.0185	0.0120	0.0233	0.0383	0.023	39
coefficients	A_2^1	0.0026	0.0018	0.0020	0.0021	0.0034	0.0024	0.0047	0.003	41
Kolosov's param.	κ	1.10	1.11	1.06	1.01	1.81	0.96	0.92	1.14*	27*
Poisson's ratio	ν_{RL}	0.475	0.473	0.486	0.498	0.297	0.510	0.520	0.47	18
Fracture	$G_{F,crit}$	219	239	178	147	188	115	166	179	23
energy	$G_{F,cum,tot}$	311	361	307	240	304	200	350	296	21
$[\frac{J}{mm^2}]$	$G_{F,cum}$	231	316	262	237	199	220	284	250	17
	$G_{F,res}$	327	355	197	231	281	230	316	277	22

* Values after discarding outlier with highest standard deviation are: κ_{mean} = 1.03 with COV = 7%.

Table 2
Fracture properties obtained from analysis of WST experiments in TL. $P_{h,max}$ - maximum splitting force, COD_{max} - crack opening displacement at maximum splitting force, SLIP - initial slip, a_{ini}- initial crack length, T_x, T_y, R -rigid body motions, A_1^1, A_2^1- first term Fourier series coefficients for deformation modes I and II respectively, K_{Ic} - mode I critical stress intensity factor. $G_{F,crit}$ - critical fracture energy, $G_{F,cum}$ - cumulative specific fracture energy, $G_{F,cum,tot}$ - total cumulative specific fracture energy, $G_{F,res}$ - fracture resistance at the final crack slope.

SPECIMEN ID: WST-SPECIMEN NO		01-TL 1	02-TL 2	03-TL 3	04-TL 4	06-TL 5	07-TL 6	09-TL 7	mean	COV [%]
$P_{h,max}$		4565	4487	4746	4747	7324	4481	4861	5030	20
$COD_{max} - SLIP$ [mm]		1.29	1.08	1.28	1.21	1.82	1.90	0.97	1.22	25
K_{Ic}	a_{ini} (DIC)	0.50	0.52	0.53	0.48	0.80	0.53	0.54	0.56	22
[MPa m$^{0.5}$]	a_{ini} = 10 mm	0.45	0.49	0.44	0.40	0.41	0.36	0.44	0.47	22
a_{ini} from DIC [mm]		20.4	25.74	22.5	14.7	20.8	27.7	35.3	23,9	19
Rigid body	T_x [mm]	0.0687	0.0132	0.0530	0.0127	0.0005	0.0002	0.0881	0.03	106
	T_y [mm]	0.1919	0.0215	0.0195	0.0804	0.0459	0.0843	0.3694	0.12	109
	R [rad]	0.0069	0.0026	0.0009	0.0015	0.0065	0.0007	0.0003	0.00	100
Def. Mode	A_1^1	0.0047	0.0183	0.0067	0.0219	0.0183	0.0221	0.0075	0.01	54
coefficients	A_2^1	0.0007	0.0023	0.0012	0.0032	0.0020	0.0020	0.0005	0.00	56
Kolosov's param.	κ	1.69	1.55	1.10	0.94	–	0.83	–	1.22	31
Poisson's ratio	ν_{TL}	0.328	0.362	0.474	0.514	–	0.542	–	0.44	21
Fracture	$G_{F,crit}$	199	217	225	181	514	226	237	257	45
energy	$G_{F,cum,tot}$	427	512	412	531	849	312	613	522	33
$[\frac{J}{mm^2}]$	$G_{F,cum}$	273	331	247	514	695	150	178	282	46
	$G_{F,res}$	349	399	272	519	530	384	545	412	25

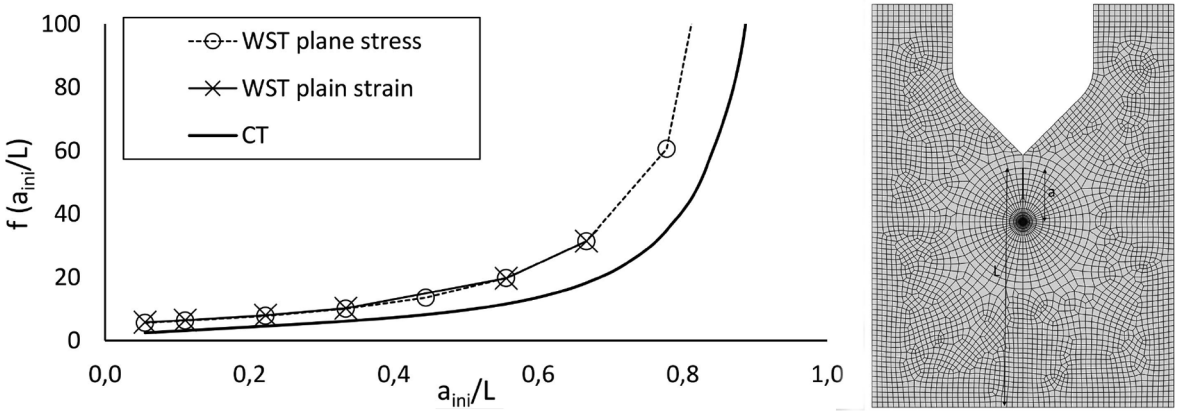

Fig. 10. The stress intensity factor solution for WST and CT tests (left) and corresponding mesh for SIF evaluation in WST specimen using contour integral in ABAQUS where $a_{ini}/L = 0.22$ (right).

$$G_{F,I} = \frac{K_I^2}{\sqrt{2E_1E_2}}\left(\sqrt{\frac{E_1}{E_2}} + \frac{E_2}{2G_{12}} - \frac{E_1\nu_{21}}{E_2}\right)^{1/2} \tag{11}$$

In the equation above, the transversely isotropic material model for wood is assumed (not entirely proper within elasticity theory because shear terms are not dependent on axial terms in stiffness matrix) and the crack propagates along the grain, thus $E_1 = E_L$, $E_2 = E_3 = E_R = E_T$, $G_{12} = G_{13} = G_{TL} = G_{RL}$, $\nu_{21} = \nu_{TL} = \nu_{RL}$. Thus, $G_{F,crit}$ is obtained from Eq. 11 by substituting K_I with $K_{I,c}$, see resulting values in Table 1.

3. Results

3.1. Deformation fields

The fitted deformation field gives information about the composition of mode I and mode II in the total kinematic response. Coefficients of the first terms of the power series, evaluated for the deformation stage corresponding to the peak force value, are summarized in Tables 1, 2. On average the ratio of A_1^1/A_2^1 is around 10 for the RL series and 9 for the TL series, which indicates that opening (mode I) related deformations are one order of magnitude larger than the shearing deformation (mode II). The corrections

for rigid body motions R are negligible compared to the typical smallest crack length value, see a_{ini} in Tables 1 and 2. The average peak force from the test series is 4.5 kN forthe RL and 5.0 kN for the TL series (4.6 kN if 06-TL specimen is disregarded) with a coefficient of variation (COV) of around 10% and 20% (3%) respectively. The optimized value of the Kolosov's parameter κ for the fields before damage initiation has a very low COV for the RL series. This corresponds to the Poisson's ratio of 0.5 on average with 7% COV, with the assumption of plane strain (the result for specimen no 5 (WST-06) were here treated as an outlier due to the first unloading-reloading cycle occurring before the test reached maximum force). The Poisson's ratio obtained in the TL series varies due to the different board sides measured for different specimens and, thus, has to be considered separately in each case.

3.2. Crack length estimation

The crack tip locations a, determined with the optimization algorithm for each deformation stage, are plotted together with force-displacement curves (as functions of COD) for each specimen in Figs. B.13 and B.14 and for selected specimens from both series in Fig. 9. The crack length curves a interact with the force-displacement curves as all drops in force values related to the unloading-reloading stages correspond to jumps in the crack length. Also naturally occurring drops in the force-displacement graph are reflected in the crack length curve as well. At the initial stage of loading, the crack tip locations are more uncertain, and this is visible in the flat curves of the error function in Fig. 7. The plateau of relatively similar values of the error function for a substantial range of crack tip positions implies that crack tip localization is sensitive to the selected error threshold in the optimization procedure. Extrema are more pronounced for higher loads values after the peak force is passed, confer Fig. 12, where error value maps are presented.

For stable parts of crack propagation a pattern of fluctuations with respect to crack length was observed in the curve, see Fig. 11. The frequency corresponds to the discretization of the deformation field. The result of the optimization procedure is hence somewhat affected by the choice of mesh used for evaluating displacements from images. The effect observed for different mesh sizes is shown in Fig. 11. Mesh of sizes of 9, 17 and 26 pixels were created for the set of images for specimen WST-04-RL. The convergence of the crack length curve can be observed for the finer DIC mesh. Also, the discretization error, apparent in the pattern of jumps corresponding to the dimensions of the mesh, is naturally decreasing with the smaller mesh size.

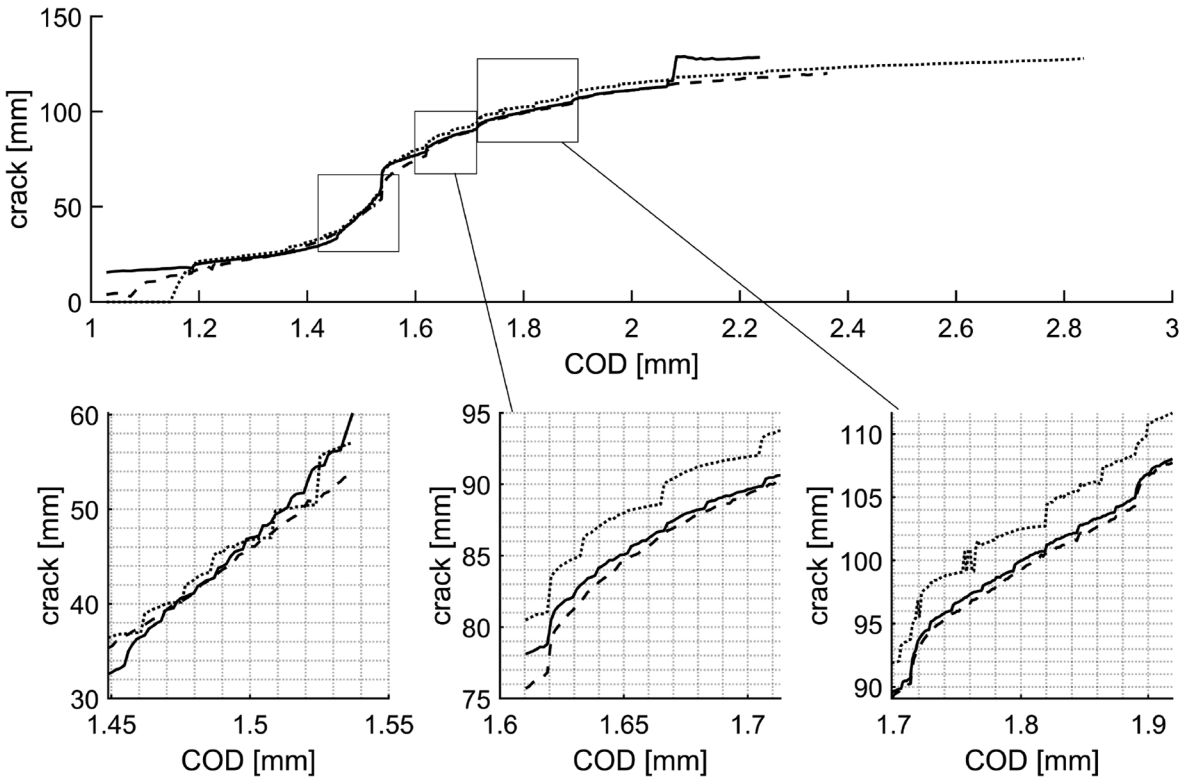

Fig. 11. Top: Examples of crack propagation curve from optimization of deformation fields based on DIC with mesh of 17 pixel (continuous line), 9 pixels (dashed line) and 26 pixels (dotted line). Bottom: zoom on selected curve parts.

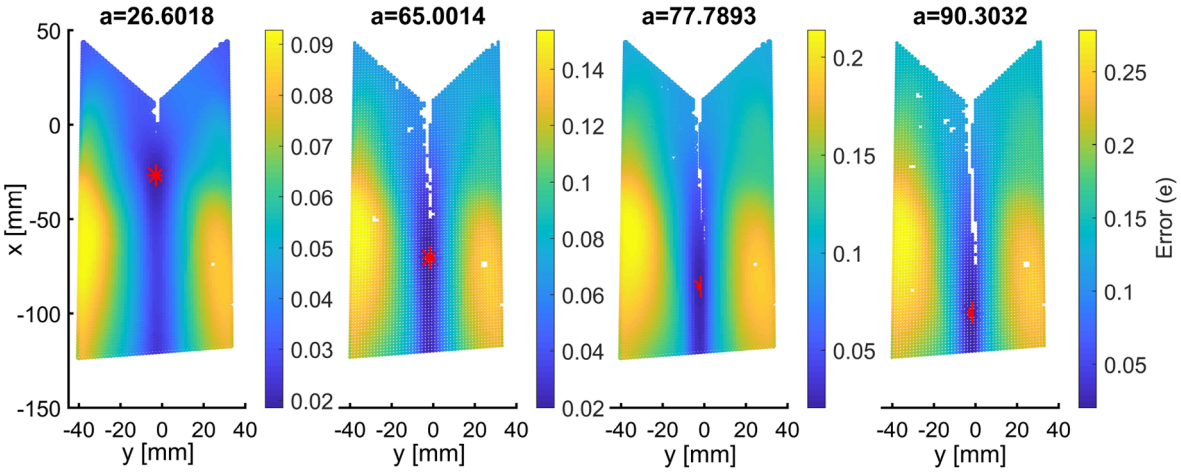

Fig. 12. Error function map, Eq. (8), for experimental deformation field at different stages of loading and crack propagation lengths in specimen WST-07. An asterisk denotes optimized crack tip localization.

Table 3
Material properties used in finite element analysis.

$E_{1=L}$	$E_{2=R=T}$	$G_{12=LR=TL}$	$\nu_{21=RL=TL}$
9040	790	640	0.11

3.3. Resistance curve

Fracture resistance curves (R-curves) are presented on the right side of Figs. 9, B.13 and B.14. Numerical differentiation of non-smooth experimental data is very sensitive to the increment selection, thus the step-wise linear approximation of differentiated curves a and G_c was chosen. R-curves are shown together with values of specific fracture energy $G_{F,cum}$ and $G_{F,cum,tot}$. The R-curves reflect the non-monotonic loading procedure and therefore need to be observed cautiously. In Tables 1, 2, the resistance $G_{F,res}$ evaluated for the final crack length section is listed. The difference between $G_{F,res}$ and $G_{F,cum}$ is about 11% and 25% for RL and TL respectively. COV for $G_{F,res}$ stays on similarly low level in both test series, 22 and 24%.

3.4. Critical stress intensity factors

The critical stress intensity factors $K_{I,c}$ are summarized in Tables 1 and 2. To account for the existence of initial crack and FBZ, the crack value obtained from optimization of the deformation field a_{ini} was directly used in the function $f(a_{ini}/L)$, which accounts for the geometry of the specimen. The critical SIF was also calculated assuming reference value $a_{ini} = 10$ mm for all specimens since machining induced, or drying cracks are usually present in the wood. SIF for DIC based a_{ini} is on average 10% higher and corresponding critical fracture energy is 20% higher. Critical fracture energy can be calculated from critical SIF with the formula given in Eq. (11). It is valid for orthotropic materials in plane-stress, but the actual cylindrical orthotropy of wood is not taken into account. The critical energies presented in Tables 1, 2 were obtained using material data from Table 3, based on [3,2]. Stress intensity factors do not depend on the actual values of material constants but on the degree of anisotropy. However, equivalent fracture energy (Eq. (11)) includes material information and thus depends on the material properties. Critical fracture energies $G_{F,crit}$ based on $K_{I,c}$ are also shown on the R-curve graph. However, it is worth remembering that in materials with fracture process zone the stress intensity factor is not a good measure of fracture toughness.

4. Discussion

4.1. Crack tip localization algorithm and results discussion

Crack tip localization based on optimization of kinematic fields provides a realistic continuous crack path. The test is non-monotonic so the total released energy is hence decreased by a lost fraction of energy stored in the FBZ. However, the unloading-

Table 4
Critical stress intensity factor ($K_{I,c}$) and specific fracture energy $G_{I,F}$ reported by different authors and in the current paper, WST- wedge split test, CT- compact tension test.

Fracture parameter:	$K_{I,C}$ [MPa m^{0,5}]	$G_{I,F}$ [kN/m]	Specimen type
Material orientation:	RL	RL	–
Tan (1995) [29]	0,45	0,266	WST
Fonselius (1992) [8]	0,25	–	CT
Stanzl-Tschegg (1994) [27]	0,55	0,245	WST
Stanzl-Tschegg (1995) [24]	0,45–0,75	0,240	WST
Stanzl-Tschegg (1996) [26]	0,405	0,186	WST
current paper	0,47(a_{ini} from DIC)	0,30 ($G_{F,res}$)	WST

reloading procedure allows observation of the damage and reconstruction of the FBZ, which is visible as peaks and drops in the resistance curve after each unloading-reloading cycle, confer Figs. B.13 and B.14 to the right. It can be observed that unloading-reloading cycles affect FBZ especially in the force region of around 75–30% of the peak force. The decreasing effect of the un-reloading cycles for very small forces can be due to the too-small amount of strain energy stored in the specimen at these stages, incapable to cause significant damage in FBZ. Force-displacement (F_h-COD) based evaluation of released energy and kinematically based (DIC) crack length a are independent, yet compatible experimental measurements.

4.2. Fracture mechanics parameters evaluation

The fracture energy evaluation based on measured crack length allows for direct quantification of the energies at different stages of loading. The method captures crack propagation jumps caused by either unloading-reloading cycles or material heterogeneity along the crack path. It is worth to mention that the current method, analysing the kinematic fields during the fracture process, allows identification of both opening and shearing mode. This is a major advantage considering the difficulties to obtain pure modes of deformation states in experimental testing of wood. The material properties obtained in the present paper have been compared to the data from the literature, see Table 4. On average, the SIF and the specific fracture energy are in good agreement with values found by other authors, considering the high variability of material properties of wood. The results for series TL were not compared here, due to the major differences in the test set-ups.

A comparison between the specific fracture energy and fracture resistance, obtained in this paper for the same specimens, show that the latter one is consistently larger. The specific fracture energy, $G_{F,cum}$ and $G_{F,cum,tot}$, was expected underestimated due to the non-monotonic procedure of loading, causing damage to the fracture process zone. However, the value of the corresponding fracture resistance obtained from the measured crack path data is larger than the specific fracture energy for WST specimen, see Tables 1, 2, which suggests that it is significantly less dependent on the unloading-reloading procedure.

5. Conclusions

In the present paper, a method for measurement of a crack path using DIC and an optimization technique for quantification of displacement fields are emphasized. The results show that the method has extended capabilities compared to other approaches, although it is complex and laborious. The crack path is obtained independently from the force-displacement measurement procedure and, thus, does not rely on indirect methods. The observed consistent difference in values of specific fracture energy and fracture resistance, suggests that the influence of the history of loading on the method is limited. The present method based on measured crack path data is found only locally sensitive to unstable force-displacement curves caused either by the chosen loading procedure or occurring naturally due to the heterogeneity in wood. Thus, a wide range of tests that are non-monotonic or only stepwise stable can be analysed and therefore, more information about the fracture process can be gained. Moreover, the method can be used to quantify the damage caused by unloading-reloading cycles and, consequently, be useful in cycling damage evaluations. The method distinguishes between opening and shearing mode and hence, it is valid for material parameter evaluations also under mixed-mode loading.

Declaration of Competing Interest

The authors declare that they have no known competing financial interests or personal relationships that could have appeared to influence the work reported in this paper.

Appendix A. Table with measurements of grain angle deviation

Variation of material properties affects the nominal testing conditions of mode I in the wedge splitting test. The presence of the shearing mode is mostly attributed to the grain angle deviation. The values of the actual angle in specimens of RL and TL series were measured after testing at 4 points across the thickness for two fracture surfaces, each on one half of the split specimen, resulting in 8 measured locations for each specimen. The data were obtained using labella. Measurements are collected in Tables A.5 and A.6.

Table A.5
Measurements of grain angle [°] for TL specimen series.

Measurement no	1	2	3	4	5	6	7	8	MEAN	ST. DEV.	COV
WST-02	2	1.9	2	0.3	1.5	2.9	0.1	0.5	1.4	1.00	0.71
WST-03	1.7	3.2	0.3	0.2	1.1	1.9	0.2	0.3	1.1	1.09	0.98
WST-04	2	2.4	1.9	0.8	2	2.5	1.3	0.9	1.7	0.65	0.38
WST-05	1	2.4	0.7	2.2	1.4	1.7	2.5	2.6	1.8	0.72	0.40
WST-06	1	0.8	0	2.4	1	0.8	1.6	2	1.2	0.76	0.64
WST-07	1.7	1.8	0.7	2.4	1.4	0.2	1.5	3	1.6	0.88	0.56
WST-08	2.2	0.7	0.8	2.5	1	0.4	1.8	3.1	1.6	0.98	0.63
TOTAL									1.5	0.87	0.58

Table A.6
Measurements of grain angle [°] for RL specimen series.

Measurement no	1	2	3	4	5	6	7	8	MEAN	ST. DEV.	COV
WST-01	1.8	3.6	3.6	3.2	1.6	2.4	2.8	3.6	2.8	0.82	0.29
WST-02	0.9	2.0	1.8	0.9	1.8	1.9	2.2	1.8	1.7	0.49	0.29
WST-03	1.9	0.2	0.1	0.6	2.0	2.5	0.8	0.7	0.8	0.76	0.95
WST-04	1	1.2	1.6	0.5	0.5	1.7	3.1	1.9	1.6	0.98	0.62
WST-06	2.8	3.9	5.3	1.2	0.9	0.8	1.5	1.5	2.6	1.60	0.61
WST-07	0.9	0.9	2.6	3.2	1.5	0.2	4.0	2.6	2.1	1.19	0.58
WST-09	2.7	0.7	1.2	1.5	0.9	0.4	1.7	1.7	1.5	0.61	0.41
TOTAL									1.9	1.14	0.61

Appendix B. Results of experiments for all RL and TL specimen series

Figs. B.13–B.16.

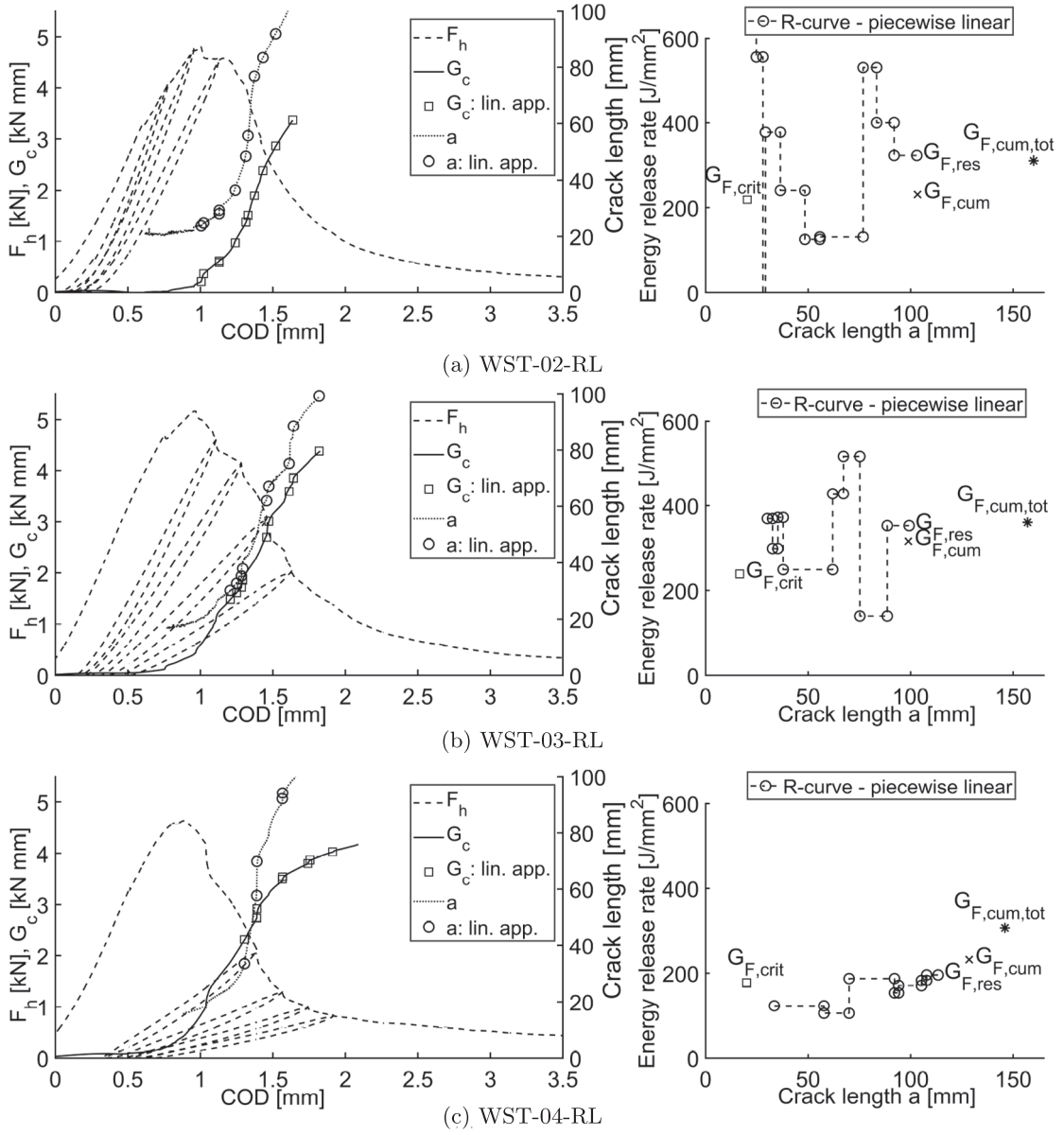

Fig. B.13. Left: Force-displacement curve, cumulative fracture energy G_c , crack length a, lin. app. - piecewise linear approximation; Right: energy release rate (R-curve).

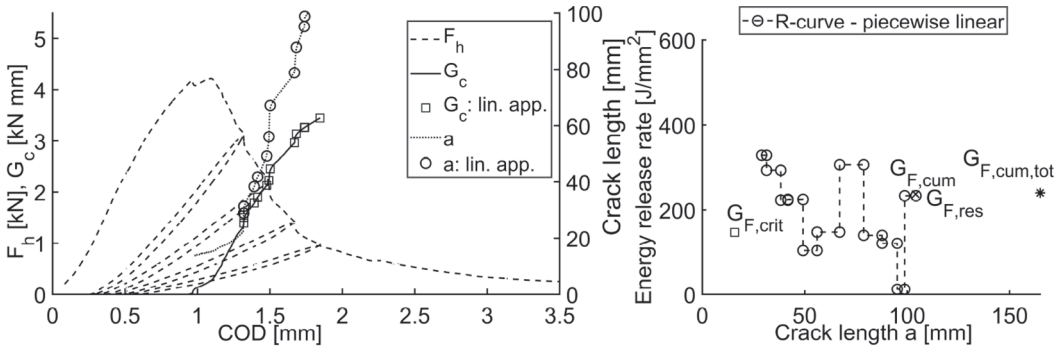

(a) WST-05-RL

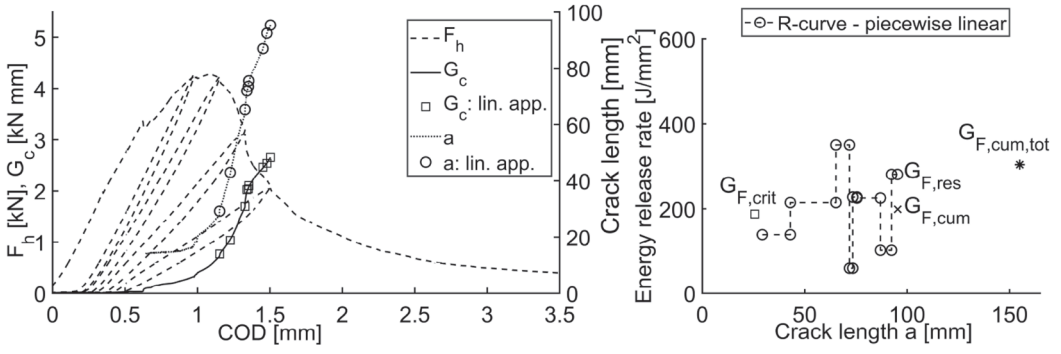

(b) WST-06-RL

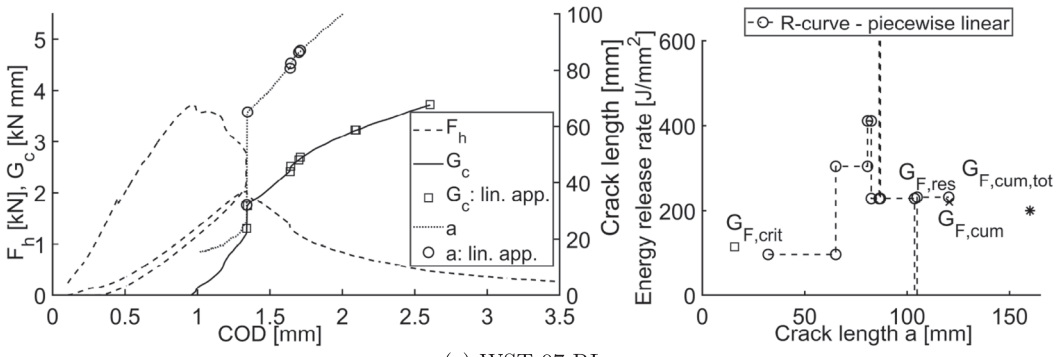

(c) WST-07-RL

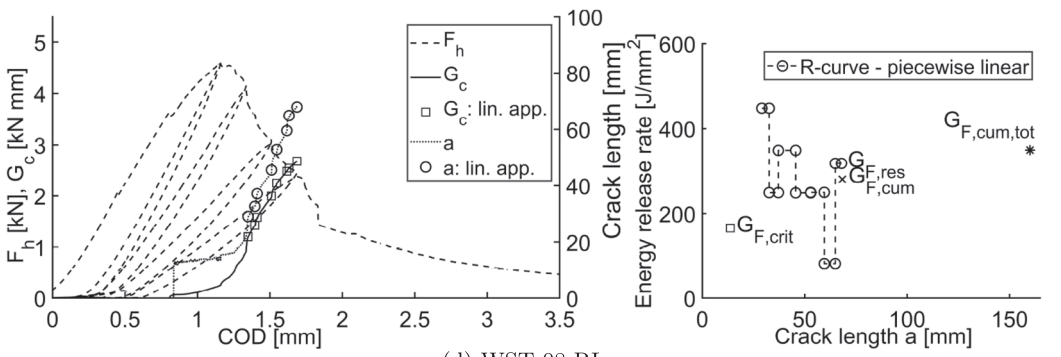

(d) WST-08-RL

Fig. B.14. Left: Force-displacement curve, cumulative fracture energy G_c, crack length a, lin. app. - piecewise linear approximation; Right: energy release rate (R-curve).

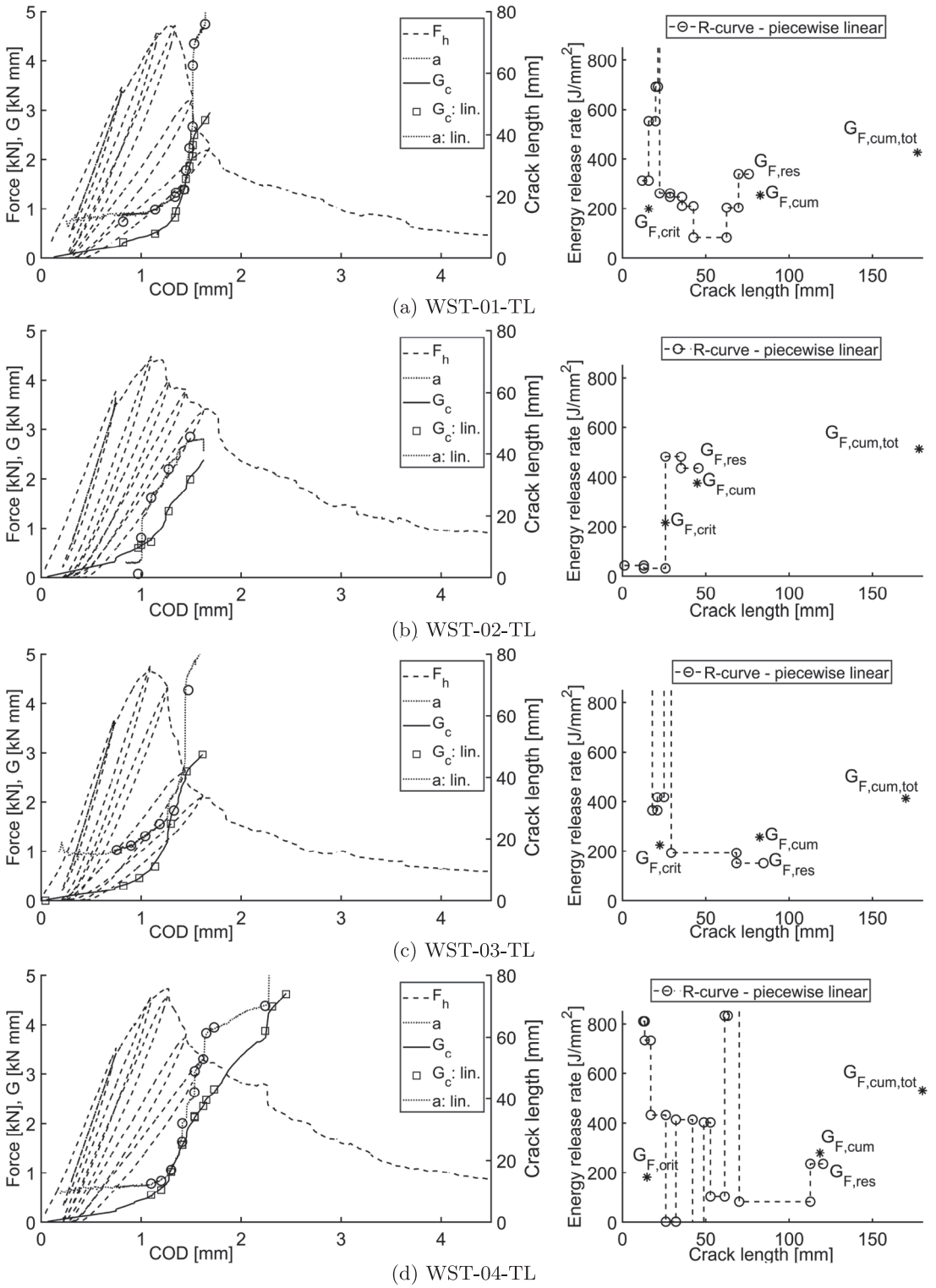

Fig. B.15. Left: Force-displacement curve, cumulative fracture energy G_c , crack length a; Right: energy release rate (R-curve).

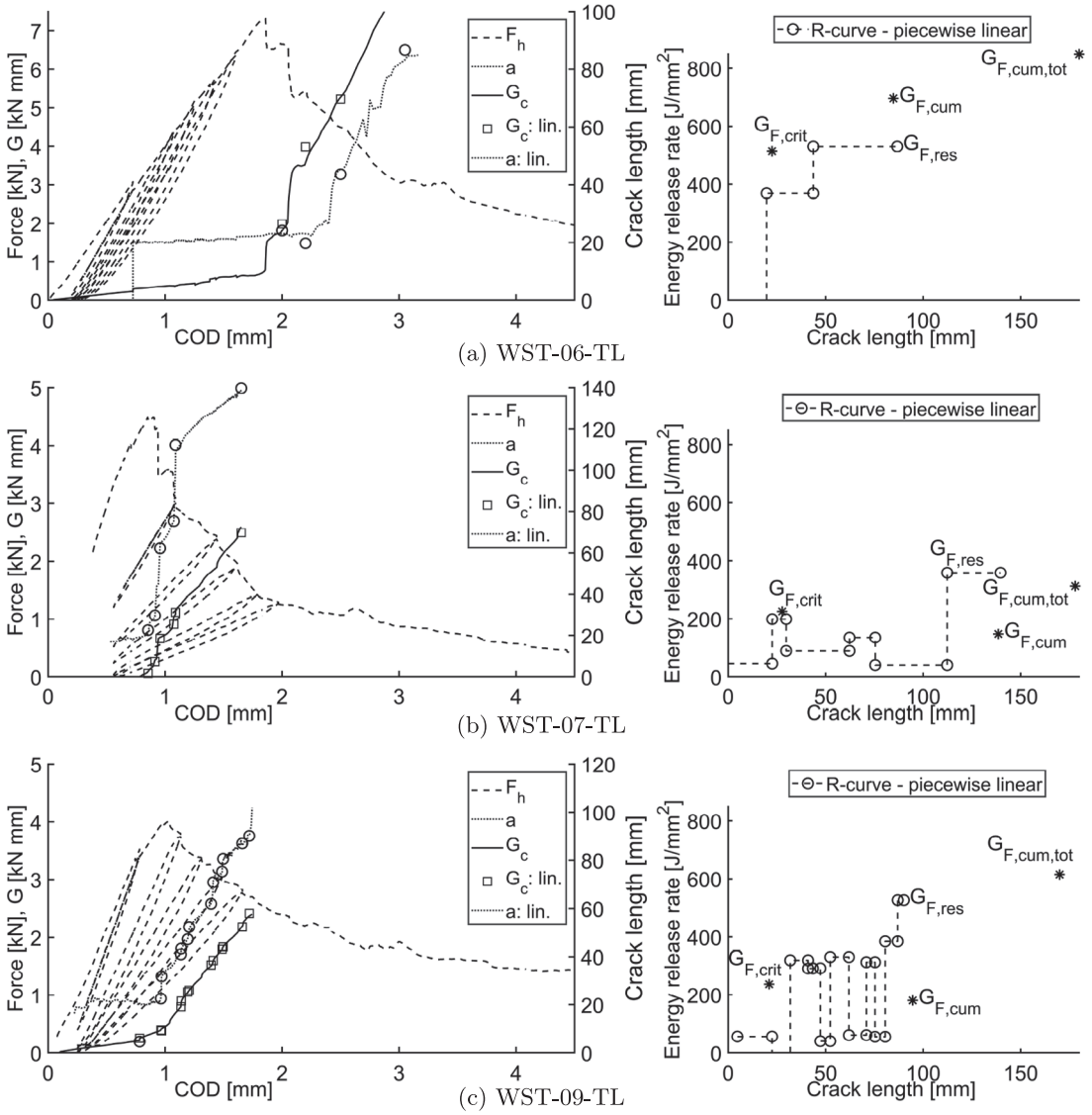

Fig. B.16. Left: Force-displacement curve, cumulative fracture energy G_c , crack length a; Right: energy release rate (R-curve).

Appendix C. Detailed results for the fitted deformation field with coefficients A for higher order terms for specimen TL-03

The power series of the Kolosov-Mushkelishvili deformation field around the crack tip is fitted with the experimental field from DIC and the coefficients for each of the N = 7 terms for both deformation modes are determined. The example of numeric results for specimen TL-03 at the load F = 5.4 kN is shown in Fig. C.17. The values of coefficients **A** are listed in Table C.7.

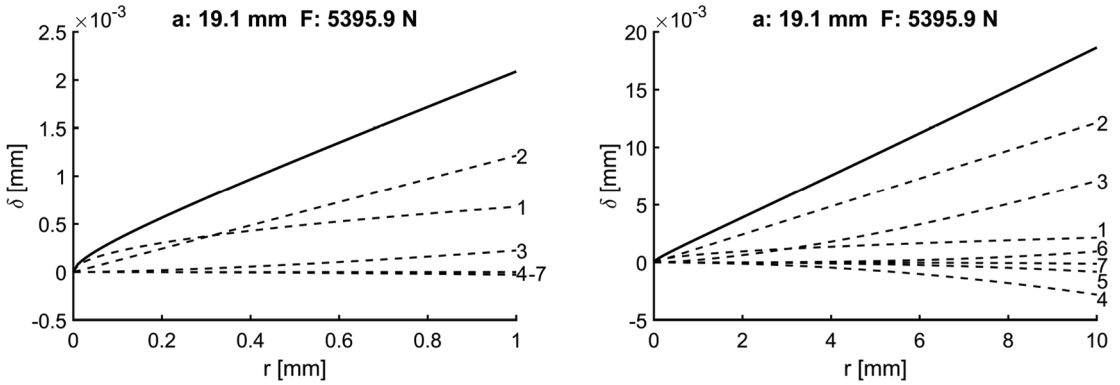

Fig. C.17. Fitted analytical mode I displacement δ (separation) along the crack lips for specimen TL-03 at force value F, crack length a, $\phi = \pi$ and r = 0–1 mm (left) and r = 0–10 mm (right). All N = 1–7 terms are shown separately (dashed curve) and the total deformation is represented by continuous line.

Table C.7
Displacement field coefficients for WST-RL-03 at F = 5.2 kN.

Mode	A^1	A^2	A^3	A^4	A^5	A^6	A^7
I	$2.11E-2$	$-1.66E-4$	$-7.19E-5$	$3.71E-6$	$-7.78E-7$	$4.05E-8$	$-2.64E-9$
II	$-1.8E-3$	$1.3E-3$	$4.50E-6$	$-4.36E-6$	$9.95E-9$	$1.06E-7$	$-3.57E-9$

References

[1] Bodig J, Jayne B. Mechanics of wood and wood composites. Malabar, Florida: Krieger Publishing Company; 1993.
[2] Dahl KB. Mechanical properties of clear wood from Norway spruce [PhD thesis]. Norwegian University of Technology, Department of Structural Engineering; 2009.
[3] Dahl KB, Malo KA. Linear shear properties of spruce softwood. Wood Sci Technol 2009;43(5):499–525.
[4] de Moura M, Silva M, de Morais A, Morais J. Equivalent crack based mode ii fracture characterization of wood. Eng Fract Mech 2006;73(8):978–93.
[5] de Moura MFSF, Dourado N. Wood Fracture Characterization 1st ed.. CRC Press; 2018.
[6] Dubois F, Méité M, Pop O, Absi J. Characterization of timber fracture using the digital image correlation technique and finite element method. Eng Fract Mech 2012;96:107–21.
[7] EN 1995-1-1: Eurocode 5. En1995-1-1, design of timber structures - part 1. Standard, European Comitee for Standarization, 2nd ed., Avenue Marnix 17, B-1000 Brussels; 1995.
[8] Fonselius M, Riipola K. Determination of fracture toughness for wood. J Struct Eng-ASCE 1992:118.
[9] Hooke R, Jeeves T. Direct search solution of numerical and statistical problems. J ACM (JACM) 1961;8(12):212–29. https://doi.org/10.1145/321062.321069. In press.
[10] Sobek J, Frantík P, Veselý V. Analysis of accuracy of Williams series approximation of stress field in cracked body – influence of area of interest around crack-tip on multi-parameter regression performance. Eng Fract Mech 2012;92:89–100.
[11] Jamaaoui A, Pop O, Dubois F, Costa G. Wedge splitting test on douglas genotypes using an integrated mixed-mode approach. Theoret Appl Fract Mech 2017;91:44–51.
[12] Linsbauer H, Tschegg E. Fracture energy determination of concrete with cube-shaped specimens. Zement und Beton 1986;31(1):38–40.
[13] Malíková L, Veselý V. Significance of higher-order terms of the Williams expansion for plastic zone extent estimation demonstrated on a mixed-mode geometry. Procedia Mater Sci 2014;3:1383–8. 20th European Conference on Fracture.
[14] Mirzaei B, Sinha A, Nairn J. Measuring and modeling fiber bridging: application to wood and wood composites exposed to moisture cycling. Compos Sci Technol 2016;128:65–74.
[15] Méité M, Dubois F, Pop O, Absi J. Mixed mode fracture properties characterization for wood by digital images correlation and finite element method coupling. Eng Fract Mech 2013;105:86–100.
[16] Méité M, Pop O, Dubois F, Absi J. Characterization of mixed-mode fracture based on a complementary analysis by means of full-field optical and finite element approaches. Int J Fract 2013;180(1):41–52.
[17] Ayatollahi MR, Akbardoost J. Size effects on fracture toughness of quasi-brittle materials – a new approach. Eng Fract Mech 2012;92:89–100.
[18] Nairn J, Matsumoto N. Fracture modeling of crack propagation in wood and wood composites including crack tip processes and fiber bridging mechanics, vol. 5; 2009. p. 12–7.
[19] NS-EN 338. Ns-en 338, structural timber - strength classes. Standard, European Comitee for Standarization, 2nd ed.; 2016.
[20] Panin SV, Chemezov VO, Lyubutin PS, Titkov VV. The algorithm of crack and crack tip coordinates detection in optical images during fatigue test. IOP Conf Ser Mater Sci Eng 2017;177(1):012019.

[21] Sih GC, Paris PC, Irwin GR. On cracks in rectilinearly anisotropic bodies. Int J Fract Mech 1965;1(3):189–203.
[22] Smith I, Landis E, Gong M. Fracture and Fatigue in Wood. Wiley; 2003.
[23] Smith M. ABAQUS/Standard User's Manual, Version 6.14. Simulia; 2014.
[24] Stanzl-Tschegg S, Tan D-M, Tschegg E. New splitting method for wood fracture characterization. Wood Sci Technol 1995;29(1):31–50.
[25] Stanzl-Tschegg SE. Microstructure and fracture mechanical response of wood. Int J Fract 2006;139(3):495–508.
[26] Stanzl-Tschegg SE, Tan DM, Tschegg EK. Fracture resistance to the crack propagation in wood. Int J Fract 1996;75(4):347–56.
[27] Stanzl-Tschegg SE, Tschegg EK, Teischinger A. Fracture energy of sprucewood after different drying procedures. Wood Fiber Sci 1994;26(4):467–78.
[28] Tada H, Paris P, Irwin G. The stress analysis of cracks handbook. third ed. John Wiley and Sons Ltd.; 2000.
[29] Tan DM, Stanzl-Tschegg SE, Tschegg EK. Models of wood fracture in mode i and mode ii. Holz als Roh- und Werkstoff 1995;53(3):159–64.
[30] Wilson E, Mohammadi M, Nairn J. Crack propagation fracture toughness of several wood species. Adv Civ Eng Mater 2013;2(1):316–27.
[31] Yoneyama S, Ogawa T, Kobayashi Y. Evaluating mixed-mode stress intensity factors from full-field displacement fields obtained by optical methods. Eng Fract Mech 2007;74(9):1399–412.
[32] Zanganeh M, Lopez-Crespo P, Tai YH, Yates JR. Locating the crack tip using displacement field data: a comparative study. Strain 2017;49(2):102–15.